Resorcinarene cavitand based morphologically distinct polymers as templates for iridium electrocatalysts

Binh Le
Advisor: Dr. Ramjee Balasubramanian
Department of Chemistry & Biochemistry, Old Dominion University, Norfolk, VA.

Abstract: Template-directed synthesis offers a promising route to morphologically controlled precious metal nanostructures that maximize active surface area and reduce precious metal utilization. This work reports the use of photopolymerized resorcinarene tetraalkene tetrathiol (RTATT) fibrous scaffolds in ethyl acetate as templates for the synthesis of palladium monometallic and palladium-iridium bimetallic nanostructures. RTATT fibers were characterized by ^{1}H NMR spectroscopy, confirming partial thiol-ene conversion. Direct synthesis of palladium nanostructures on unfunctionalized and 1-hexene-functionalized RTATT fibers was investigated across two Pd to S ratios, revealing a strong dependence of nanoparticle distribution and aggregate morphology. Palladium-iridium bimetallic nanostructures were subsequently prepared through galvanic exchange of the Pd-RTATT fiber composites with iridium(III) chloride, and the role of bromide in galvanic exchange reaction was assessed. TEM and EDS characterization confirmed substantial galvanic displacement of palladium by iridium, yielding densely packed nanoparticles of 2 to 6 nm distributed along the fiber scaffold.

Introduction

Proton exchange membrane water electrolysis (PEMWE) has emerged as the leading electrochemical technology for converting water to hydrogen and oxygen PEMWE offers distinct advantages including high current density operation and compact system design. In PEMWE systems, water oxidation proceeds at the anode through the oxygen evolution reaction (OER), while hydrogen evolution occurs concurrently at the cathode. The OER constitutes the thermodynamically and kinetically unfavorable half-reaction and thereby represents the rate-limiting step that governs the overall efficiency of the electrolysis process. Consequently, improvements in OER catalytic activity, current efficiency, and operational stability are critical to enhancing PEMWE system performance and enabling practical deployment of water electrolysis technology.

Iridium-based catalysts represent the current state-of-the-art for oxygen evolution reaction catalysis in PEMWE systems, having achieved unparalleled activity and stability across diverse operational environments.[1] The exceptional performance of iridium catalysts derives from their ideal binding energy for oxygen-containing intermediates, their ability to sustain electrochemical activity across broad temperature and pH ranges, and their remarkable corrosion resistance in the acidic, oxidative conditions inherent to the anode environment of proton exchange membrane electrolyzers.[1] However, the widespread deployment of iridium-based OER catalysts is fundamentally constrained by two interconnected challenges: the extreme scarcity of iridium as a naturally occurring element and its correspondingly high market cost. Annual global iridium production reaches only approximately seven to nine tons rendering it among the rarest elements on Earth and creating severe supply limitations for large-scale electrolyzer manufacturing.[2] Furthermore, conventional iridium-based OER catalysts require substantial precious metal loadings at the anode, typically ranging from 2.0 to 3.0 milligrams of iridium per square centimeter of electrode surface, which significantly elevates the capital cost of water electrolysis systems and undermines their economic viability for widespread adoption.[3] The United States Department of Energy has established ambitious technical targets to address this constraint, specifying a reduction in total platinum group metal content in PEM electrolyzers from current levels of 3.0 milligrams per square centimeter to 0.5 milligrams per square centimeter by 2026, with an ultimate target of 0.125 milligrams per square centimeter by 2030, while simultaneously maintaining performance standards and durability requirements.[4] These aggressive reduction targets necessitate fundamental advances in iridium nanostructure design and catalyst morphology optimization that maximize atomic efficiency and exploit the electrochemically active surface area without compromising the inherent catalytic performance and stability characteristics that distinguish iridium among precious metal catalysts.

In response to these stringent precious metal loading constraints and the fundamental necessity for enhanced catalyst efficiency, two complementary strategies have emerged from recent literature to simultaneously improve iridium catalyst activity while substantially reducing the required precious metal content: the incorporation of secondary metals through compositional alloying and the deliberate engineering of nanostructure morphology to maximize surface utilization.[5] The introduction of foreign metals into iridium-based catalysts via alloying has been shown to modify both the electronic and geometric properties of the active sites, thereby tuning the binding energy of oxygen-containing reaction intermediates and improving overall oxygen evolution kinetics. The alloying approach functions through a synergistic mechanism in which

secondary metals induce a shift in the d-band center of iridium, thereby optimizing the adsorption and desorption kinetics of reaction intermediates while simultaneously reducing the total mass of precious metal required per unit catalytic performance.[6]

Concurrent with advances in compositional control through alloying, the morphological engineering of iridium nanostructures has emerged as an equally powerful approach to maximize electrochemically active surface area and thereby enhance the intrinsic utilization of precious metal atoms.[5] One-dimensional nanostructures such as nanowires and nanodendrites offer substantial advantages due to their high aspect ratios, large exposed surface areas, and preferential exposure of active crystallographic facets.[7] Two-dimensional morphologies including nanosheets similarly maximize surface exposure while offering unique electronic properties arising from their planar geometry.[7] By synergistically combining compositional control through transition metal alloying with morphological engineering at the nanoscale, researchers have achieved substantial reductions in iridium loading from conventional levels of 2.0 to 3.0 milligrams per square centimeter down to 0.35 milligrams per square centimeter while simultaneously maintaining or enhancing overall catalytic activity and operational stability.[8] These advances demonstrate that precise control of both nanostructure geometry and elemental composition represents a promising and feasible materials chemistry approach to addressing the cost and scarcity constraints that presently limit large-scale deployment of PEMWE technology.

Template-directed synthesis has emerged as a powerful and versatile methodology to direct the growth of inorganic nanostructures into predetermined morphologies with excellent size uniformity and well-defined crystallographic properties.[9] Recent advances in template-directed synthesis have demonstrated transformative catalytic benefits for precious metal nanostructures across multiple systems.[10-12] A notable recent advancement employed a poly(styrene)-block-poly(vinylpyridine)-block-poly(ethylene oxide) triblock copolymer as a structure-directing agent to synthesize dendritic high-entropy alloy nanoparticles incorporating iridium alongside platinum, palladium, silver, and ruthenium, with the block copolymer serving as a confined nucleation template that promoted single-phase formation and uniform metal distribution while enabling facile removal through simple solvent extraction post-synthesis.[13] Furthermore, comprehensive studies on block copolymer template-directed synthesis of ordered metallic nanostructures have established methodologies for fabricating two-dimensional metal nanosheets with iridium and other precious metals, demonstrating that the architectural control afforded by block copolymer self-assembly can be effectively extended across an entire class of catalytically significant metals to produce well-defined, replicable nanostructures unattainable through conventional synthetic approaches.[14] These recent demonstrations establish that template-directed approaches provide not just marginal improvements but rather transformative enhancements in catalyst utilization and performance, particularly when soft polymeric templates are employed to enable precise compositional and morphological control of precious metal nanostructures.

Our research group has established a direct, template- and surfactant-free approach to the synthesis of morphologically tunable polymeric nanostructures through the thiol-ene photopolymerization of resorcinarene tetra alkene tetra thiol (RTATT) a cavitand monomer (Figure 1).[15]

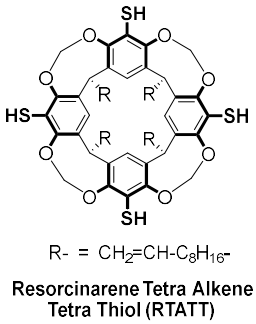

Figure 1. Resorcinarene tetra alkene tetra thiol cavitand (RTATT).

Upon UV irradiation at 254 nm and 300 nm, RTATT undergoes free radical thiol-ene photopolymerization through a step-growth mechanism initiated by homolytic cleavage of the sulfur-hydrogen bond to generate a thiyl radical, which adds across a pendant alkene group and propagates through sequential chain transfer to regenerate the thiyl radical.[16] The identity of the photopolymerization solvent exerts decisive control over the morphology of the resulting polymer architecture: irradiation in chloroform yields hollow nanocapsules with an average diameter of approximately 106 nm, irradiation in ethyl acetate produces fibers and extended interconnected fibrous network structures approximately 50 nm in width, and irradiation in tetrahydrofuran and dichloromethane affords polydisperse nanoparticles and distorted honeycomb-like lattice structures respectively, demonstrating that a broad range of polymeric nanostructure geometries are accessible from a single monomer through systematic variation of reaction solvent alone. At relatively shorter irradiation duration, in addition to the formation of the sulfide linkages resulting from thiol-ene photopolymerization, residual unreacted thiol and alkene groups are also observed.

The sulfide linkages and thiol functional groups inherent to the RTATT polymer scaffold provide

multivalent binding sites capable of stabilizing metal nanoparticles both inside and outside the polymer shell. Our group showed that RTATT nanocapsules could direct the synthesis of gold nanostructures through a modified Brust-Schiffrin approach (Figure 2), with the morphology of the resulting product depending critically on reaction conditions, particularly the sulfur to metal salt ratio; specifically, continuous gold nanoshells approximately 12 nm in thickness form at a sulfur-to-gold molar ratio of 0.5, while spherical aggregates of closely packed individual nanoparticles form at a sulfur-to-gold molar ratio of 0.8.[17] The nanocapsule-templated gold nanoparticle aggregates demonstrated catalytic utility in a model reduction reaction. Further, work from our lab has also shown that this approach can be extended to the assembly of platinum nanoparticles inside RTATT nanocapsules.[18]

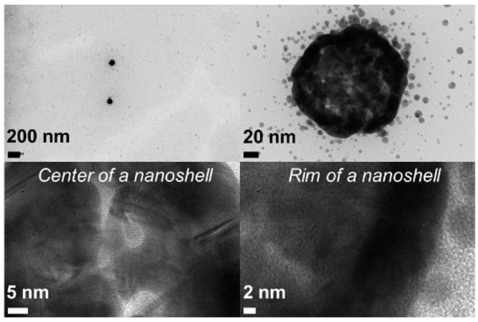

Figure 2. TEM analysis of gold nanostructures prepared with photopolymerized RTATT nanocapsule as templates.[17]

Unpublished work from our group also showed that fibers and fibrous network structures generated by photopolymerization of RTATT in ethyl acetate, could also be used to template gold nanostructures (Figure 3). Interestingly, these structures showed the formation of both relatively smaller spherical nanoparticles and anisotropic gold nanostructures.

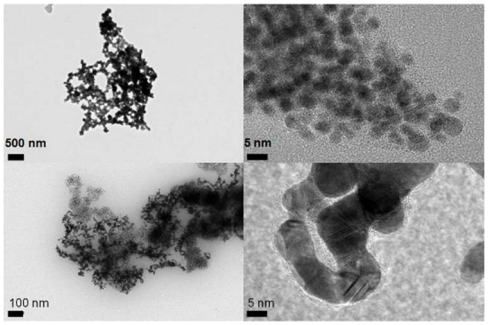

Figure 3. TEM analysis of gold nanostructures prepared with RTATT fiber as templates.

The focus of this work is to utilize RTATT fibers and fibrous networks as templates for synthesizing one- and two- dimensional Ir nanostructures, with the goal of developing highly efficient electrocatalysts for OER in PEMWE systems. This work reports the RTATT fiber-templated synthesis of palladium monometallic and palladium-iridium bimetallic nanostructures. Photopolymerized RTATT fibers in ethyl acetate were employed as templates for the direct synthesis of palladium nanostructures, where the impact of Pd to S ratio and fiber surface functionalization on the resulting nanoparticle morphology and distribution was examined systematically. Palladium-iridium bimetallic nanostructures were subsequently formed through galvanic exchange reactions, where the role of bromide was also investigated.

Experimental

General remarks: Resorcinol (MP Biomedicals), 10-undecanal (>95%, Aldrich), bromochloromethane (98%, SynQuest Labs), n-butyllithium (2.5M, Aldrich), sodium tetrachloropalladate (98%, Aldrich) tetraoctylammonium bromide (Aldrich), tetrabutylammonium bromide (>98%, Aldrich), sodium borohydride (99% Thermo Scientific), iridium(III) chloride hydrate (TCI), 1-hexene (97%, Acros), and 200 proof ethanol (Decon Laboratories) were used as received. Prior to use, N-bromosuccinimide (99%, Acros) was recrystallized, cesium carbonate (99%, Alfa Aesar) was activated under vacuum with heating for at least 24 h and elemental sulfur was sublimed. THF and toluene were dried under standard conditions. Synergy ultrapure water (18.2 MΩ cm) was used for all reactions. Photopolymerizations were carried in a Srinivasan-Griffin Rayonet photochemical reactor. The reactor was equipped with four 254 nm and four 300 nm lamps, supplied by the Southern New England Ultraviolet Company.

Synthesis of RTATT fibers: RTATT was dissolved in distilled ethyl acetate and filtered through a 0.45 micron nylon filter into a quartz tube. The contents were degassed with argon for 30 seconds and sealed. The sealed quartz tube was irradiated for varying time periods.

Functionalization of RTATT fibers with 2-mercaptoethylamine hydrochloride: To the RTATT fibers obtained after 15 min of photopolymerization, 4 equivalents of 1-hexene was added and the solution was degassed with argon for 30 seconds. The mixture was irradiated for 30 min. Four equivalents of 2-mercaptoethylamine hydrochloride in 1 mL ethanol was added to the quartz tube and the contents degassed with argon for 30 seconds then irradiated for an additional 30 min under the same conditions. The product was purified by two rounds of centrifugation (9000 rpm, 20 min) precipitation and redispersion with ethanol.

Functionalization of RTATT fibers 11-mercaptoundecyl-N,N,N-trimethylammonium bromide: To the RTATT fibers obtained after 15 min of photopolymerization, 2 equivalents of 11-mercaptoundecyl-N,N,N-trimethylammonium bromide was added and the solution degassed with argon for 30 seconds. The mixture was irradiated for 30 min. Four equivalents of 1-hexene was then added to the quartz tube, the contents degassed with argon for 30 seconds then irradiated for an additional 30 min under the same conditions. The product was purified by centrifugation and precipitation with ethanol.

Synthesis of monometallic Pd nanostructures with RTATT: To an aqueous solution of Na_2PdCl_4 (0.0179 g, 0.0609 mmol Pd), a solution of tetraoctylammonium bromide (0.102 g, 0.186 mmol) in 10 mL ethyl acetate was added and vigorously stirred under argon for 30 min. The organic phase containing phase transferred metal salt was isolated and combined with RTATT-fibers in ethyl acetate (9 mL, 1.5 mM of monomer, 1.1 equivalents of Pd to S) obtained after 15 min of photopolymerization and stirred under argon for an additional 30 min. The reaction mixture was cooled in an ice bath for 5 min, and aqueous solution of ice cold $NaBH_4$ (0.443 M, 2 mL) was added and the mixture was stirred under argon at 0°C for 1 h. The product was washed with water (3 x 10 mL). A similar reaction was also carried out in the presence of 1-hexene functionalized RTATT fibers under identical conditions.

To probe the effect of concentration on the resulting Pd nanoparticles this procedure was carried out in the presence of RTATT fibers in ethyl acetate (9 mL, 0.75 mM of monomer, 2.3 equivalents of Pd to S), under otherwise identical conditions.

Synthesis of PdIr bimetallic nanostructures by galvanic exchange reaction: To a 3 mL aliquot of Pd nanoparticles prepared in the presence of RTATT fibers in ethyl acetate, tetrabutylammonium bromide (454 mg, 1.408 mmol) was added, followed by the addition of $IrCl_3$ (3.3 mg in 3 mL of ethanol) and refluxed under argon. The product was purified by two rounds of centrifugation at 9000 rpm for 20 min and precipitation with ethanol. This procedure was also carried out in the absence of tetrabutylammonium bromide to evaluate its effect on the resulting nanoparticles.

Results and Discussion

RTATT cavitand was synthesized in four steps as shown in Scheme 1 according to the methods described in previous work.[15] Briefly, resorcinarene was obtained by the acid promoted condensation of resorcinol and 11-undecenal, which was subsequently brominated with N-bromosuccinimide. Bromoresorcinarene cavitand was obtained with bromochloromethane in the presence of cesium carbonate under sealed tube conditions. Bromoresorcinarene cavitand was treated with n-BuLi, followed by treatment with elemental sulfur to yield RTATT.

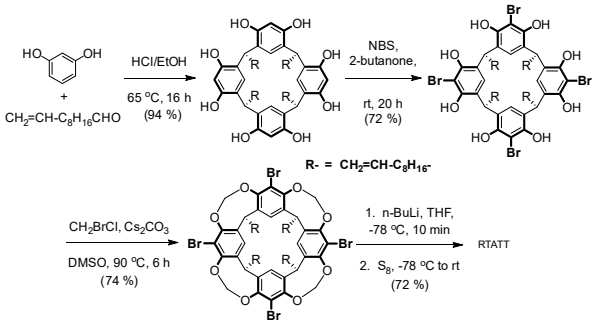

Scheme 1. Synthesis of RTATT.

To probe the impact of RTATT concentration on the morphology of the resulting polymers, 0.5 mM and 3 mM solutions of RTATT in ethyl acetate were photopolymerized for 1 h and 0.5 h respectively. Longer duration at higher concentrations sometimes led to turbid solutions or sheet like 2D structure formation. Comparison of the ^{1}H NMR spectra of the RTATT monomer and the photopolymerized product in $CDCl_3$ (Figure 4) revealed the substantial broadening of the peaks in the latter and further attenuation of the terminal alkene signals at ~ 5.7 and 4.9 ppm, and the thiol signal at ~ 3.8 ppm in the photopolymer relative to the monomer. Both observations are consistent with partial consumption of the alkene and thiol functional groups during photopolymerization, with unreacted alkene and thiol groups retained within the polymer scaffold.

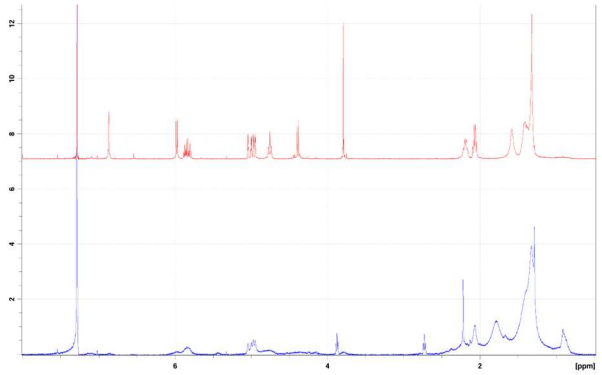

Figure 4. NMR spectra of RTATT monomer (top, red) and RTATT fiber/fibrous networks (0.5 mM initial concentration, 1 h of photopolymerization).

TEM analysis of these photopolymerized samples (Figure 5) showed the presence of both fibers and fibrous network structures consistent with the results obtained from the previous work[19] albeit in various proportions. These fibers typically had a width of ~ 50

nm.[16] Qualitatively, longer individual fibers (up to 350 nm in length) were observed along with some fibrous network structures at lower monomer concentration while higher proportion of network structures along with somewhat shorter fibers (up to 200 nm) were observed at higher concentration.

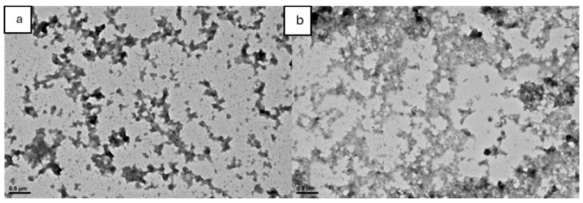

Figure 5. TEM analysis of photopolymerizations carried out in ethyl acetate with a) 0.5 mM (1 h) and b) 3.0 mM (0.5 h) RTATT monomer concentrations.

Consistent with the earlier reports from our group[19, 20], occasionally turbidity or precipitation of the photopolymers formed in ethyl acetate was observed under certain conditions. However, the polymers formed after 15 min of photoirradiation were clear. Work from our group has shown that the development of distinct morphology including fibers and fibrous networks occurs as early as 15 min.[16] Given this, we chose 15 min as the duration of the initial photopolymerization prior to further functionalization. Also, with the presence of higher proportion of residual thiol and ene functional groups earlier in these reactions, maximum functionalization is expected under these conditions.

These fibers and fibrous network structures were functionalized with both 1- hexene and thiols such as 2-mercaptoethylamine hydrochloride or 11-mercaptoundecyl-N,N,N-trimethylammonium bromide to orthogonally functionalize residual thiol and ene functional groups. Both these thiols were insoluble in ethyl acetate and required the addition of ethanol as a co-solvent. When the thiol functionalization was carried out first, the RTATT fibers and fibrous network showed some turbidity or precipitation, with the shorter chain thiol showing more precipitation. As expected, fibers functionalized with longer thiols showed better solubility. To further improve the solubility and reduce the amount of residual thiol in these fibers, 1-hexene functionalization was also carried out. The amounts of these functionalizing agents were also varied. The process of optimization of the extent of functionalization without compromising on the solubility is currently underway in our laboratory.

Unfunctionalized RTATT fibers were employed as templates for the direct synthesis of monometallic Pd under modified Brust-Schiffrin conditions. Briefly, a mixture of TOA^+ stabilized PdX_4^{2-} in ethyl acetate was reduced with aqueous sodium borohydride in the presence of the RTATT fibers at 0 °C for 1 h. Consistent with literature reports[21], the Pd to S proportion was maintained at 1 or above. At a Pd to S ratio of 1.1, TEM analysis revealed the formation of amorphous aggregates in which Pd nanoparticles were distributed nonuniformly throughout the fibrous polymer template (Figure 6). At higher magnification, Pd nanoparticles can be seen nucleating preferentially along the fibrous polymer template in a distinctive chain-like arrangement which suggests growth-directing influence from the fiber polymer template. Furthermore, the presence of both larger anisotropic nanostructures and smaller isotropic nanoparticles were observed.

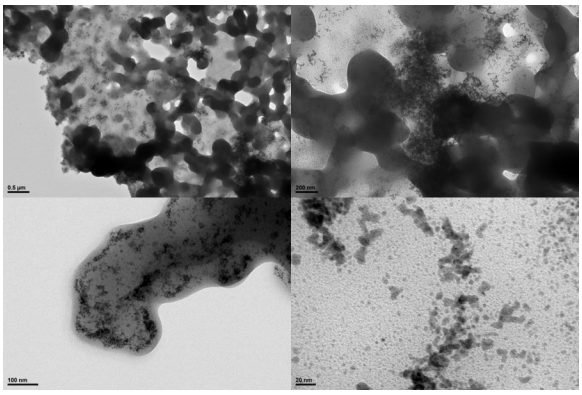

Figure 6. TEM analysis of Pd nanostructures synthesized with RTATT fibers at a Pd to S ratio of 1.1 at 0 °C for 1 h.

In addition to the expected Pd, the EDS analysis of these nanoparticles revealed the presence of both S and Br (Figure 7).

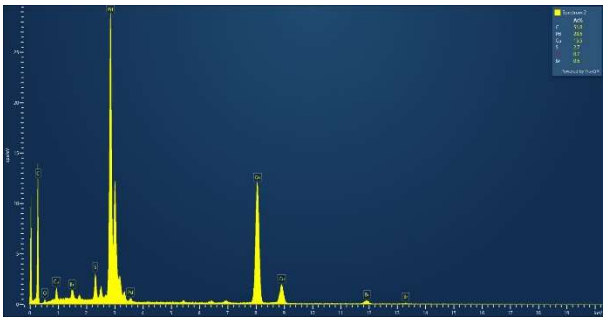

Figure 7. EDS analysis of Pd nanoparticles formed in the presence of Pd to S ratio of 1.1 at 0 °C for 1 h.

Even in dark areas where there were no nanoparticles, EDS analysis revealed the presence of Pd, S and Br under these reduction conditions, perhaps indicating the incomplete reduction of Pd salt under these conditions, which also explains the presence of unusual dark areas without nanoparticles.

To probe the role of residual thiols remaining in these templates, RTATT photopolymer fibrous networks functionalized with 4 equivalents of 1-hexene were employed as templates for the direct synthesis of Pd nanostructures under similar conditions Preliminary

evaluation by TEM (Figure 8) revealed that they were very similar to those obtained in the presence of unfunctionalized fibers, though qualitatively not many anisotropic nanostructures could be observed in the former.

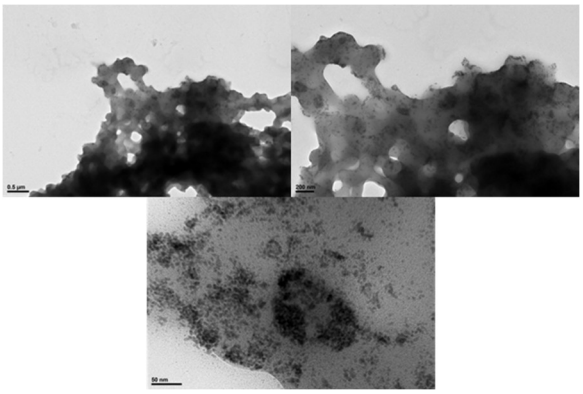

Figure 8. TEM analysis of Pd nanostructures synthesized with 1-hexene functionalized RTATT fibers at a Pd to S ratio of 1.2 at 0 ºC for 1 h.

When a Pd to S ratio of 2.3 was employed, TEM analysis revealed a markedly different morphology characterized by a substantially higher density of Pd nanoparticles distributed more uniformly throughout the fibrous polymer template (Figure 9). The particles forms a dense colony of discrete particles, continuously coating along the fiber network rather than isolated aggregated clusters.

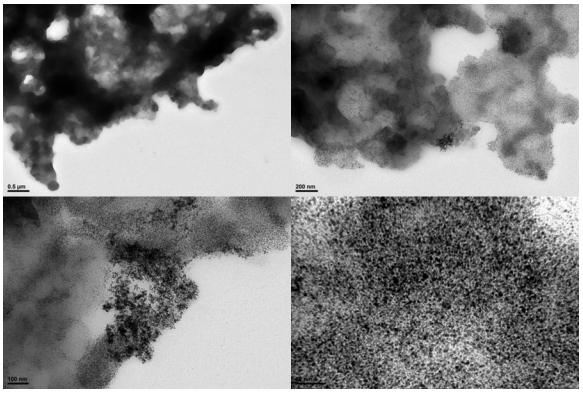

Figure 9. TEM analysis of Pd nanostructures synthesized with RTATT fibers at a Pd to S ratio of 2.3 at 0 ºC for 1 h,

Galvanic exchange reaction of Pd with Ir was carried out by adapting a literature procedure developed by Xia and coworkers.[22] They carried out galvanic exchange reaction at 130 ºC in ethylene glycol in the presence of KBr. Given the limited dispersion of these nanostructures in ethylene glycol or ethanol, an ethyl acetate – ethanol binary solvent system was employed along with tetrabutylammonium bromide as the bromide source. The TEM analysis of these nanostructures appeared somewhat similar to their parent palladium nanostructures (Figure 10). These nanoparticles also had darker patches.

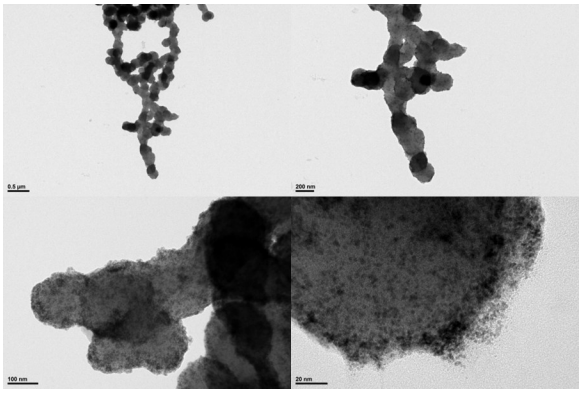

Figure 10. TEM analysis of PdIr bimetallic nanostructures synthesized via galvanic exchange of RTATT fiber-templated Pd nanostructures with $IrCl_3$ in the presence of tetrabutylammonium bromide.

The EDS analysis of an individual nanoparticle formed under these conditions clearly showed the significant exchange of Pd by Ir, along with some amount of S and Br (Figure 11).

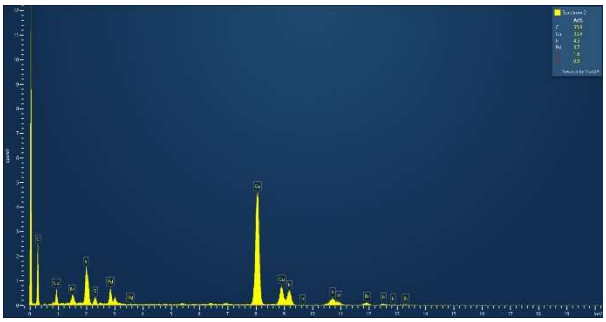

Figure 11. EDS analysis of an individual nanoparticle obtained after galvanic exchange reaction in the presence of tetrabutylammonium bromide.

However, the EDS analysis of the intense dark region showed the substantial presence of Br and S when compared to Pd and Ir (Figure 12).

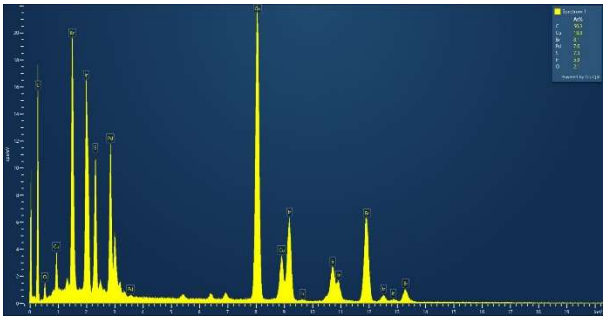

Figure 12. EDS analysis of the intense dark bulk region of the galvanic exchange reaction product obtained in the presence of tetrabutylammonium bromide.

Remarkably, when the galvanic exchange reaction was carried out in the absence of the bromide source under otherwise identical conditions, the TEM analysis of the product

obtained clearly revealed presence of expected RTATT fibrous morphology, with a densely packed, nearly continuous coating of nanoparticles distributed uniformly along the fiber scaffold (Figure 13). Further the intense dark patches observed in the other TEMs were absent under these conditions.

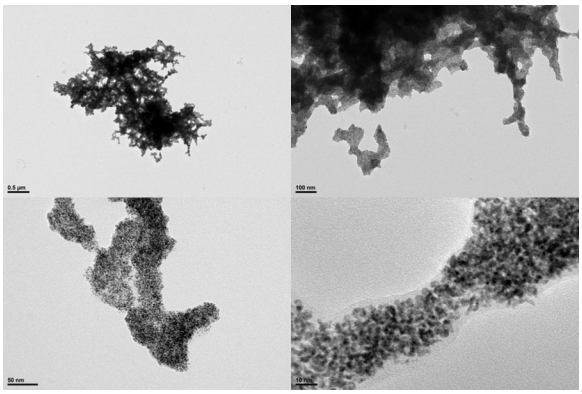

Figure 13. TEM analysis of PdIr bimetallic nanostructures synthesized via galvanic exchange of RTATT fiber-templated Pd nanostructures with $IrCl_3$.

EDS analysis confirmed the presence of both Ir and Pd along with a reduced amount of Br.

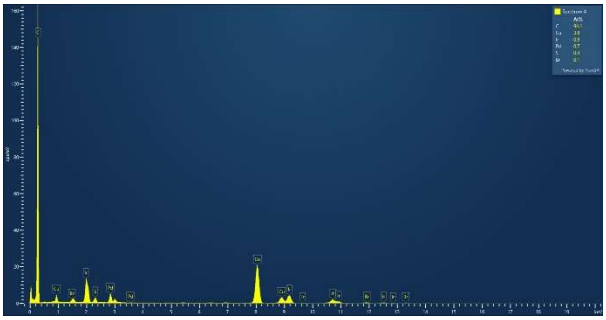

Figure 14: EDS analysis of PdIr bimetallic structure synthesized in the absence of tetrabutylammonium bromide.

Conclusion

The fibers and fibrous network structures obtained from the photopolymerization of resorcinarene tetraalkene tetrathiol cavitand were employed as templates for the synthesis of palladium monometallic and palladium-iridium bimetallic nanostructures. The Pd to S ratio governs nanoparticle distribution and aggregate morphology within the fiber network, with higher ratio promoting more uniform nanoparticle dispersion along the scaffold. Galvanic exchange of Pd-RTATT fiber composites with $IrCl_3$ afforded PdIr bimetallic nanostructures with confirmed iridium incorporation by EDS, yielding densely packed 2 to 6 nm nanoparticles along the fiber scaffold under bromide-free conditions. Collectively, these results establish RTATT fibrous scaffolds as a versatile and chemically tunable template for bimetallic precious metal nanostructure synthesis and support the broader application of this platform toward the development of morphologically controlled iridium-based catalysts for oxygen evolution in proton exchange membrane water electrolysis. Currently direct synthesis of iridium nanostructures with functionalized RTATT fibers is underway in our laboratory.

References

(1) Galyamin, D.; Tolosana-Moranchel, Á.; Retuerto, M.; Rojas, S. Unraveling the Most Relevant Features for the Design of Iridium Mixed Oxides with High Activity and Durability for the Oxygen Evolution Reaction in Acidic Media. *JACS Au* **2023**, *3* (9), 2336-2355. DOI: 10.1021/jacsau.3c00247.

(2) Smith, B., Graziano, D., Riddle, M., Liu, D.-J., Sun, P., Iloeje, C., Kao, E., & Diamond, D. (2022). Platinum Group Metal Catalysts: Supply Chain Deep Dive Assessment. https://doi.org/10.2172/1871583

(3) Knöppel, J.; Möckl, M.; Escalera-López, D.; Stojanovski, K.; Bierling, M.; Böhm, T.; Thiele, S.; Rzepka, M.; Cherevko, S. On the limitations in assessing stability of oxygen evolution catalysts using aqueous model electrochemical cells. *Nature Communications* **2021**, *12* (1), 2231. DOI: 10.1038/s41467-021-22296-9.

(4) https://www.energy.gov/eere/fuelcells/technical-targets-proton-exchange-membrane-electrolysis

(5) Wang, H.; Li, X.; Zhang, G.; Gu, Z.; Chen, H.; Wei, G.; Shen, S.; Cheng, J.; Zhang, J. Recent Progress in Balancing the Activity, Durability, and Low Ir Content for Ir-Based Oxygen Evolution Reaction Electrocatalysts in Acidic Media. *Small* **2025**, *21* (6), 2410407. DOI: https://doi.org/10.1002/smll.202410407.

(6) Wu, Q.; Gao, Q.; Wang, X.; Qi, Y.; Shen, L.; Tai, X.; Yang, F.; He, X.; Wang, Y.; Yao, Y.; et al. Boosting electrocatalytic performance via electronic structure regulation for acidic oxygen evolution. *iScience* **2024**, *27* (1), 108738. DOI: 10.1016/j.isci.2023.108738 From NLM.

(7) Wang, C.; Feng, L. Recent advances and perspectives of Ir-based anode catalysts in PEM water electrolysis. *Energy Advances* **2024**, *3* (1), 14-29, 10.1039/D3YA00492A. DOI: 10.1039/D3YA00492A.

(8) Peng, X.; Satjaritanun, P.; Taie, Z.; Wiles, L.; Keane, A.; Capuano, C.; Zenyuk, I. V.; Danilovic, N. Insights into Interfacial and Bulk Transport Phenomena Affecting Proton Exchange Membrane Water Electrolyzer Performance at Ultra-Low Iridium Loadings. *Advanced Science* **2021**, *8* (21), 2102950. DOI: https://doi.org/10.1002/advs.202102950.

(9) Sun, Z.; Wang, S.; Hu, X. Polymer-Functionalized Nanocatalysts: Engineering Interfaces and Microenvironments for Enhanced Catalysis. In *Polymers*, 2026; Vol. 18, p 465.

(10) Takimoto, D.; Toma, S.; Suda, Y.; Shirokura, T.; Tokura, Y.; Fukuda, K.; Matsumoto, M.; Imai, H.; Sugimoto, W. Platinum nanosheets synthesized via

topotactic reduction of single-layer platinum oxide nanosheets for electrocatalysis. *Nature Communications* **2023**, *14* (1), 19. DOI: 10.1038/s41467-022-35616-4.
(11) Ando, S.; Yamamoto, E.; Kobayashi, M.; Osada, M. Atomic Layer Engineering of Pd Nanosheets for an Enhanced Hydrogen Evolution Reaction. *Nano Letters* **2024**, *24* (36), 11239-11245. DOI: 10.1021/acs.nanolett.4c02741.
(12) Ye, Z.; Chen, C.; Su, Y.; Feng, J.; Yin, Y. Templating Methods for Materials Fabrication Across Scales. *Chemical Reviews* **2026**, *126* (2), 717-798. DOI: 10.1021/acs.chemrev.5c00709.
(13) Kc, B. R.; Yusa, S.-i.; Bastakoti, B. P. Facile One-Pot Block Copolymer-Mediated Solvothermal Approach for Synthesis of High-Entropy Alloy with Enhanced OER Activity. *Precision Chemistry* **2026**, *4* (2), 165-172. DOI: 10.1021/prechem.5c00094.
(14) Jiang, B.; Guo, Y.; Kim, J.; Whitten, A. E.; Wood, K.; Kani, K.; Rowan, A. E.; Henzie, J.; Yamauchi, Y. Mesoporous Metallic Iridium Nanosheets. *Journal of the American Chemical Society* **2018**, *140* (39), 12434-12441. DOI: 10.1021/jacs.8b05206.
(15) Balasubramanian, R.; Kalaitzis, Z. M.; Cao, W. Solvent dependent morphologies in thiol-ene photopolymerization: A facile route to the synthesis of resorcinarene nanocapsules. *Journal of Materials Chemistry* **2010**, *20* (31), 6539-6543, 10.1039/C0JM00085J. DOI: 10.1039/C0JM00085J.
(16) Kalaitzis, Zaharoula M.. "Solvent Dependent Morphologies in Thiol-ene Photopolymerization: A Facile Route to Synthesis of Resorcinarene Nanocapsules" (2009). Master of Science (MS), Thesis, Chemistry & Biochemistry, Old Dominion University, DOI: 10.25777/a5aq-kh51
https://digitalcommons.odu.edu/chemistry_etds/124
(17) Balasubramanian, R.; Prayakarao, S.; Han, S.; Cao, W. Tunable gold nanostructures with nanocapsules as template reaction vessels. RS*C Advances 20***12,** 2 *(*31), 11668-11671, 10.1039/C2RA21986G. DOI: 10.1039/C2RA21986G.
(18) Han, Sangbum. "Synthesis, Morphological Control, Dispersion Stabilization and In Situ Self-Assembly of Noble Metal Nanostructures Using Multidentate Resorcinarene Surfactants" (2016). Doctor of Philosophy (PhD), Dissertation, Chemistry & Biochemistry, Old Dominion University, DOI: 10.25777/6th7-js72
https://digitalcommons.odu.edu/chemistry_etds/9
(19) Balasubramanian, R.; Kwon, Y.-G.; Wei, A. Encapsulation and functionalization of nanoparticles in crosslinked resorcinarene shells. Jou*rnal of Materials Chemistry 200***7, 1**7 *(1*), 105-112, 10.1039/B614295H. DOI: 10.1039/B614295H.
(20) Balasubramanian, R.; Kalaitzis, Z. M. Template-Free Synthesis and <italic>in Situ</italic> Functionalization of Nanocapsules. In Amp*hiphiles: Molecular Assembly and Applications, A*CS Symposium Series, Vol. 1070; American Chemical Society, 2011; pp 263-276.
(21) Zamborini, F. P.; Gross, S. M.; Murray, R. W. Synthesis, Characterization, Reactivity, and Electrochemistry of Palladium Monolayer Protected Clusters. Lang*muir 200***1, 1**7 *(2*), 481-488. DOI: 10.1021/la0010525.
(22) Cheng, H.; Wang, C.; Qin, D.; Xia, Y. Galvanic Replacement Synthesis of Metal Nanostructures: Bridging the Gap between Chemical and Electrochemical Approaches. Acc*ounts of Chemical Research 202***3, 5**6 *(7*), 900-909. DOI: 10.1021/acs.accounts.3c00067.